Parallel-mode scanning optical sectioning using digital Fresnel holography with three-wave interference phase-shifting

Roy Kelner[1,*] and Joseph Rosen[1,2]

[1]*Department of Electrical and Computer Engineering, Ben-Gurion University of the Negev, P.O. Box 653, Beer-Sheva 8410501, Israel*
[2]*rosen@ee.bgu.ac.il*
[*]*kelnerr@post.bgu.ac.il*

Abstract: The Fresnel incoherent correlation holography (FINCH) method is applicable to various techniques of imaging, including fluorescence microscopy. Recently, a FINCH configuration capable of optical sectioning, using a scanning phase pinhole, has been suggested [Optica **1**, 70 (2014)]. This capability is highly important in situations that demand the suppression of out-of-focus information from the hologram reconstruction of a specific plane of interest, such as the imaging of thick samples in biology. In this study, parallel-mode scanning using multiple phase pinholes is suggested as a means to shorten the acquisition time in an optical sectioning FINCH configuration. The parallel-mode scanning is enabled through a phase-shifting procedure that extracts the mixed term of two out of three interfering beams.

References and links

1. J. Rosen and G. Brooker, "Digital spatially incoherent Fresnel holography," Opt. Lett. **32**(8), 912–914 (2007).
2. I. Yamaguchi and T. Zhang, "Phase-shifting digital holography," Opt. Lett. **22**(16), 1268–1270 (1997).
3. A. W. Lohmann, "Wavefront reconstruction for incoherent objects," J. Opt. Soc. Am. **55**(11), 1555–1556 (1965).
4. G. Cochran, "New method of making Fresnel transforms with incoherent light," J. Opt. Soc. Am. **56**(11), 1513–1517 (1966).
5. M. K. Kim, "Full color natural light holographic camera," Opt. Express **21**(8), 9636–9642 (2013).
6. O. Cossairt, N. Matsuda, and M. Gupta, "Digital refocusing with incoherent holography," in *Proceedings of IEEE International Conference on Computational Photography* (ICCP, 2014).
7. B. Katz and J. Rosen, "Could SAFE concept be applied for designing a new synthetic aperture telescope?" Opt. Express **19**(6), 4924–4936 (2011).
8. Y. Kashter, Y. Rivenson, A. Stern, and J. Rosen, "Sparse synthetic aperture with Fresnel elements (S-SAFE) using digital incoherent holograms," Opt. Express **23**(16), 20941–20960 (2015).
9. M. K. Kim, "Adaptive optics by incoherent digital holography," Opt. Lett. **37**(13), 2694–2696 (2012).
10. J. Rosen and G. Brooker, "Non-scanning motionless fluorescence three-dimensional holographic microscopy," Nat. Photonics **2**(3), 190–195 (2008).
11. P. Bouchal and Z. Bouchal, "Wide-field common-path incoherent correlation microscopy with a perfect overlapping of interfering beams," J. Eur. Opt. Soc: Rapid Pub. **8**, 13011 (2013).
12. T. Yanagawa, R. Abe, and Y. Hayasaki, "Three-dimensional mapping of fluorescent nanoparticles using incoherent digital holography," Opt. Lett. **40**(14), 3312–3315 (2015).
13. J. Rosen, N. Siegel, and G. Brooker, "Theoretical and experimental demonstration of resolution beyond the Rayleigh limit by FINCH fluorescence microscopic imaging," Opt. Express **19**(27), 26249–26268 (2011).
14. P. Bouchal, J. Kapitán, R. Chmelík, and Z. Bouchal, "Point spread function and two-point resolution in Fresnel incoherent correlation holography," Opt. Express **19**(16), 15603–15620 (2011).
15. X. Lai, S. Zeng, X. Lv, J. Yuan, and L. Fu, "Violation of the Lagrange invariant in an optical imaging system," Opt. Lett. **38**(11), 1896–1898 (2013).
16. J. Rosen and R. Kelner, "Modified Lagrange invariants and their role in determining transverse and axial imaging resolutions of self-interference incoherent holographic systems," Opt. Express **22**(23), 29048–29066 (2014).
17. X. Lai, S. Xiao, Y. Guo, X. Lv, and S. Zeng, "Experimentally exploiting the violation of the Lagrange invariant for resolution improvement," Opt. Express **23**(24), 31408–31418 (2015).

18. R. Kelner, J. Rosen, and G. Brooker, "Enhanced resolution in Fourier incoherent single channel holography (FISCH) with reduced optical path difference," Opt. Express **21**(17), 20131–20144 (2013).
19. D. Weigel, H. Babovsky, A. Kiessling, and R. Kowarschik, "Widefield microscopy with infinite depth of field and enhanced lateral resolution based on an image inverting interferometer," Opt. Commun. **342**, 102–108 (2015).
20. G. Brooker, N. Siegel, J. Rosen, N. Hashimoto, M. Kurihara, and A. Tanabe, "In-line FINCH super resolution digital holographic fluorescence microscopy using a high efficiency transmission liquid crystal GRIN lens," Opt. Lett. **38**(24), 5264–5267 (2013).
21. P. Bouchal and Z. Bouchal, "Non-iterative holographic axial localization using complex amplitude of diffraction-free vortices," Opt. Express **22**(24), 30200–30216 (2014).
22. R. Kelner, B. Katz, and J. Rosen, "Optical sectioning using a digital Fresnel incoherent-holography-based confocal imaging system," Optica **1**(2), 70–74 (2014).
23. M. Minsky, "Memoir on inventing the confocal scanning microscope," Scanning **10**(4), 128–138 (1988).
24. N. Siegel and G. Brooker, "Improved axial resolution of FINCH fluorescence microscopy when combined with spinning disk confocal microscopy," Opt. Express **22**(19), 22298–22307 (2014).
25. P. K. Rastogi, "Phase shifting applied to four-wave holographic interferometers," Appl. Opt. **31**(11), 1680–1681 (1992).
26. M. A. Volynsky and I. P. Gurov, "Investigation of three-beam interference fringes with controllable phase shift of two reference waves," Proc. SPIE **7790**, 779015 (2010).
27. E. Shtraikh, M. Zieder, R. Kelner, and J. Rosen, "In-line digital holography using adaptive phase pinhole on the Fourier plane," Asian J. Phys. **24**(12) 2015, in press.
28. P.-C. Sun and E. N. Leith, "Broad-source image plane holography as a confocal imaging process," Appl. Opt. **33**(4), 597–602 (1994).
29. P. C. Sun and E. Arons, "Nonscanning confocal ranging system," Appl. Opt. **34**(7), 1254–1261 (1995).
30. R. Chmelík and Z. Harna, "Parallel-mode confocal microscope," Opt. Eng. **38**(10), 1635–1639 (1999).

1. Introduction

Fresnel incoherent correlation holography (FINCH) has been introduced almost a decade ago as a method for recording Fresnel holograms under spatially incoherent illumination [1]. Utilizing modern electro-optical devices, such as spatial light modulators (SLMs) and digital image sensors, together with phase-shifting techniques [2], FINCH has given a new birth to the classical concept of self-interference-based incoherent holography [3,4] into the era of digital holography. The ability to encode information from a three-dimensional (3-D) scene or object into a single hologram, without special types of illumination (such as a laser), and later focus into various planes through digital reconstruction of the hologram, using a relatively simple - and thus elegant - apparatus, is indeed appealing. The concepts of FINCH have soon been adapted to configurations for natural day-light holography [5,6], synthetic aperture imagers [7,8], adaptive optics [9] and microscopy [10–12].

The reliance of FINCH upon self-interference goes hand in hand with its suitability for recording holograms of fluorescent objects. FINCH also offers enhanced lateral resolution, in the sense that while the cut-off frequency of its modulation transfer function (MTF) is the same as the cut-off frequency of an incoherent imaging system of similar numerical aperture, the shape of the MTF is similar to that of a coherent imaging system, which is uniform throughout the passed frequencies, and does not decay non-zero frequencies like in an incoherent imaging system [13]. This property is entangled with FINCH ability to violate the well-known Lagrange invariant [14–17], a characteristic that is also found in the closely related Fourier incoherent single channel holography (FISCH) method [18]. A recently suggested microscopy method that is based on 180° rotational shearing interferometry, similarly in part to FISCH, also exhibit this type of resolution enhancement [19]; however, unlike FISCH and FINCH, it cannot maintain depth information. Overall, the characteristics of FINCH render it applicable to biological microscopy [20]. A recently developed technique for axial localization has been successfully demonstrated in FINCH, and is capable of real-time tracking of particles [21]. Still, the limited axial resolution of FINCH [16] may diminish its usefulness for examining thick samples.

Lately, a configuration of FINCH that is capable of optical sectioning, for the imaging of thick objects, has been suggested [22]. The solution relies on the integration of a new electro-optical element into FINCH, referred to as a phase pinhole; its role is thoroughly explained in Section 2. By optionally adding point-wise illumination, a complete confocal solution may be formed, following the principles of confocal scanning microscopy [23]. Another confocal

configuration of FINCH soon followed [24]. In the latter configuration, a relay system was positioned right after the objective lens of the system, thus forming an intermediate image plane of the target object. Within that plane, a Nipkow spinning disk was inserted to provide optical sectioning before light even reaches the actual holographic interferometer (i.e., before any splitting of waves occurs). In a sense, this may be considered an off the shelf, readily available solution to optical sectioning, but it is a successful testament that a confocal FINCH system can be made competitive with conventional confocal systems in terms of lateral resolution, sectioning performance and applicability. A major drawback of these two solutions for optical sectioning using FINCH is the requirement of a scanning procedure. In the latter case [24], the scanning is mechanical but is rather quick due to the use of the Nipkow spinning disk. In the former, the scanning does not involve any mechanical movements; yet, it was only demonstrated with a rather slow point-by-point scanning [22]. In this paper, a more efficient scanning scheme is presented, where multiple points are scanned in parallel. Furthermore, a generalized phase-shifting procedure between three or more interfering waves for extracting a desired interference pattern between two waves is presented, offering the possibility of overcoming difficulties due to nonindeality of the electro-optical liquid crystal devices in use, such as the limited fill factor of SLMs. Techniques that involve phase-shifting of more than a single wave in processes of multiple wave interference were described in the past (e.g., [25,26]), and a procedure akin to the hereby described procedure have been used by us in a recent publication [27], in the context of coherent holography. However, its generalization and use in the above context of incoherent holography may have special importance. We note that methods of spatially incoherent holography that allow confocal-like optical sectioning without any scanning (for a specific plane of interest) do exist [28–30]. However, unlike [22], they are unfortunately not suitable for fluorescence imaging [30] or situations in which the user does not have control over the illumination.

2. Methods

2.1 Optical sectioning using FINCH

A schematic of an optical sectioning Fresnel incoherent correlation holography (OS-FINCH) setup is presented in Fig. 1. It is assumed that spatially incoherent light is emitted from (or scattered by) the targeted object, meaning that the object can be considered as a collection of many point sources, where the degree of mutual coherence between each pair of points is zero. Under this assumption, each point source only contributes to its own self-interference pattern, and the recorded hologram is a summation over the intensities of all self-interference patterns.

The FINCH setup in Fig. 1 is configured as a common-path single channel interferometer. This interferometer has only a single arm, and interference occurs between waves that travel along a similar direction, in a shared physical space. Consider a single point source a_o within the complete object. Two images of this point source are formed by the interferometer: the image point a_1 is formed by an imaging system that consists of two refractive lenses, the objective lens L_o and the converging lens L_c, and one diffractive lens that is realized using the left-most SLM, SLM_1; the image point a_2 is formed by an imaging system that only consists of the objective lens L_o and the converging lens L_c. The coexistence of these two imaging system is made possible due to the use of a phase-only SLM, which is an electronically controlled birefringence device. Considering linearly polarized light, polarization components oriented along the active axis of the SLM are modulated, whereas orthogonal components, oriented along the non-active axis of the SLM, are not affected by the SLM. In Fig. 1, the polarizer P_1 is set with its transmission axis oriented at a 45° angle to the active axis of the SLM, thereby allowing the simultaneous formation of the two image points a_1 and a_2. Over the image sensor plane, two spherical waves that originate from the point source a_o exist: one diverging from the image point a_1, and one converging towards the image point a_2. According to [13], a complete overlap between the two spherical waves on the image sensor guarantees

optimal image resolution. A second polarizer P_2 is positioned in front of the image sensor, with its transmission axis in parallel to the first polarizer P_1, so that the two waves can interfere over the image sensor plane. The intensity of the interference pattern encodes both the point source position in space and the point source intensity.
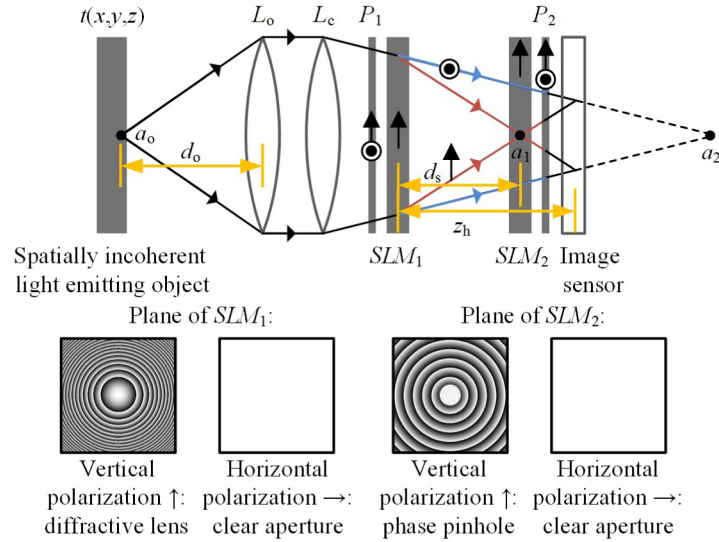

Fig. 1. Schematic of an optical sectioning FINCH setup: L_o, objective lens; L_c, converging lens; P_1 and P_2, polarizers; SLM_1 and SLM_2, spatial light modulators; a_o, point source; a_1 and a_2, point source images.

In order to achieve optical sectioning, a second phase-only SLM, SLM_2, is incorporated into the system, positioned after SLM_1 (Fig. 1). The two SLMs are positioned with their active axes in parallel, meaning that, ideally, SLM_2 does not influence the wave that is converging towards the image point a_2. SLM_2 enables optical sectioning by acting as a pinhole for the image that is formed on its surface. This image is imaged by the two refractive lenses, L_o and L_c, and the diffractive lens displayed on SLM_1. The idea behind the proposed approach of optical sectioning [22] is to preserve all (or most) of the information acquired through the interference pattern between the waves associated with the image points a_1 and a_2 (representing the point source a_o), while eliminating all (or most) of the information from other point sources. This is achieved by using SLM_2 as a phase pinhole. The phase pinhole mask is composed of two components [22]: a small circular region that is set to one of several values of uniform phase modulation, and an axicon that surrounds the phase pinhole. The latter component is used to deflect light away from the digital sensor, as an alternative to actual light blockage that occurs with an ordinary pinhole, while the former is set to three different values of phase modulation, to enable phase-shifting within the effective aperture of the pinhole.

The mechanism of the phase pinhole based optical sectioning is explained with the help of Fig. 2. For simplicity, only three point sources are considered: a_o, b_o and c_o. It is further assumed that the phase pinhole mask is centered along the image point a_1. Let $\exp(i\theta_k)A_1$, $\exp(i\theta_k)B_1$ and $\exp(i\theta_k)C_1$ denote the spherical waves that diverge away from the image points a_1, b_1 and c_1, respectively, over the image sensor plane, where $\exp(i\theta_k)$ denotes a phase-shifting constant, usually with $\theta_k = 2\pi(k-1)/3$, for $k = 1,2,3$. Additionally, let A_2, B_2 and C_2 denote the spherical waves that converge towards the image points a_2, b_2 and c_2, respectively, over the image sensor plane. A single recorded FINCH hologram, for the three point sources a_o, b_o and c_o can be described as:

$$I\left(x,y;\{a_o,b_o,c_o\}\right) = \left|e^{i\theta_k}A_1 + A_2\right|^2 + \left|e^{i\theta_k}B_1 + B_2\right|^2 + \left|e^{i\theta_k}C_1 + C_2\right|^2. \qquad (1)$$
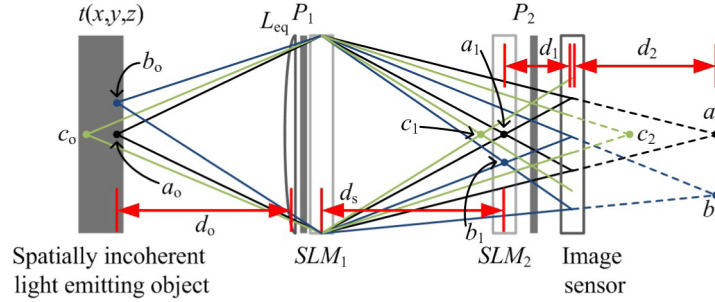
Fig. 2. Principle of optical sectioning using a phase pinhole in FINCH: L_{eq}, an equivalent lens, representing both the objective lens L_o and the converging lens L_c (Fig. 1); P_1 and P_2, polarizers; SLM_1 and SLM_2, spatial light modulators; a_o, b_o, and c_o, point sources; a_1, b_1, c_1, a_2, b_2, and c_2, point source images.

In a non-sectioning FINCH setup, a phase-shifting procedure is used to extract a final complex-valued hologram that is free from the twin-image and zeroth order terms. The actual phase-shifting is performed using SLM_1 (which, in this case, is the only SLM in the system). The final complex hologram can be described as:

$$H\left(x, y;\{a_o, b_o, c_o\}\right) = A_1 A_2^* + B_1 B_2^* + C_1 C_2^*. \tag{2}$$

In an OS-FINCH setup [22], however, the first SLM, SLM_1, is not used for phase-shifting (letting $\theta_k = 0°$), which is now performed at the small circular region of the second SLM, SLM_2. Figure 2 depicts a situation for which the spherical wave A_1 passes entirely within the phase pinhole, the spherical wave B_1 passes entirely outside of the phase pinhole, and the spherical wave C_1 only passes partially within the phase pinhole. Neglecting the impact of the axicon mask, a single recorded FINCH hologram can be described as:

$$I\left(x, y;\{a_o, b_o, c_o\}\right) = \left|e^{i\phi_l} A_1 + A_2\right|^2 + \left|B_1 + B_2\right|^2 + \left|e^{i\phi_l} S(C_1) C_1 + \left[1 - S(C_1)\right] C_1 + C_2\right|^2. \tag{3}$$

where $\phi_l = 2\pi(l - 1) / 3$, for $l = 1,2,3$, is the phase modulation value within the phase pinhole, and $S(C_1)$ is a support function that indicates the region over the image sensor in which the spherical beam C_1 is phase modulated by the phase pinhole. Following the complete phase-shifting procedure the final FINCH hologram is:

$$H\left(x, y;\{a_o, b_o, c_o\}\right) = A_1 A_2^* + S(C_1) C_1 C_2^*. \tag{4}$$

Comparing Eq. (2) and Eq. (4), for the situation described in Fig. 2, reveals that: information regarding the point source a_o is preserved; information regarding the point source b_o is eliminated; information regarding the point source c_o is partly eliminated, since the effective aperture of its hologram is greatly reduced. That is, only a specific point of interest is properly encoded into the hologram in the proposed procedure, while other points are either completely eliminated or are diminished in intensity. The result is an effective optical sectioning, but in order to record an entire 3-D object, a scanning scheme is required. Note that the result shown in Eq. (4) also holds for the case in which the effect of the axicon that surrounds the phase pinhole is considered. The use of the axicon may benefit the recording process by allowing better usage of the dynamic range of the image sensor. Further, it contributes to the elimination of undesired interference processes in which beams that ideally should not exist are involved, as discussed in Section 2.3.

The scanning procedure for a complete object, occupying a 3-D space, is performed through electrical manipulations of the SLM displayed masks, and does not involved any mechanical intervention. For simplicity, it is assumed that the two refractive lenses, L_o and L_c, and the left-most SLM, SLM_1, all lie within a common x-y plane, as shown in Fig. 2. In

practice, this is not the case, though it can be achieved using relay systems. The lens L_{eq} is an equivalent lens that represents the objective lens L_o and the converging lens L_c (Fig. 1), and its focal length $f_{eq} = f_o f_c / (f_o + f_c)$, where f_o and f_c are the focal lengths of the lenses L_o and L_c, respectively. Let d_s denote the distance between the two SLMs, SLM_1 and SLM_2, and f_1 the focal length of the diffractive lens displayed on SLM_1. The scanning procedure can be performed by considering different transverse planes of interest. Let d_o denote the distance between a specific plane of interest and the objective lens. This plane of interest should be imaged to the plane of SLM_2, which is achieved by setting the focal length of the lens displayed on SLM_1 to:

$$f_1 = \frac{d_o d_s f_{eq}}{d_s f_{eq} + d_o f_{eq} - d_o d_s}. \tag{5}$$

During the scanning procedure, the phase pinhole is laterally shifted to various positions within the plane of SLM_2, until the entire area of interest is covered. Reconstruction of a single point source is performed using its corresponding FINCH hologram, and can be done through Fresnel back-propagation to a distance which is dependent upon the distance d_o. The images of a single point source are formed at distances of d_1 and d_2 to the left and right of the image sensor, respectively. It is easy to show these two distance are:

$$d_1 = z_h - d_s, \, d_2 = d_t - z_h, \tag{6}$$

where $d_t = f_{eq} d_o / (d_o - f_{eq})$, and $z_h = 2 d_s f_c / (d_s + f_c)$ is the distance between SLM_1 and the image sensor, which assures a complete overlap between a pair of interfering spherical waves on the image sensor, for any point source located at the front focal plane of the objective lens. The reconstruction distance used for the Fresnel back-propagation is:

$$d_{rec} = \frac{d_1 d_2}{d_2 + d_1}. \tag{7}$$

Let $H_{x_o, y_o, d_o}(x, y)$ denote a FINCH hologram recorded for a point source located at (x_o, y_o), a distance d_o from the objective lens. Its reconstruction can be calculated as:

$$h_{x_o, y_o, d_o}(x, y) = H_{x_o, y_o, d_o}(x, y) * Q(1/d_{rec}), \tag{8}$$

where $Q(s) = \exp[i\pi s\lambda^{-1}(x^2 + y^2)]$ is a quadratic phase function, and * denotes a two-dimensional convolution. In order to form a reconstruction of an entire scanned plane, the reconstructions [Eq. (8)] should be combined. This can be achieved by assigning to each (x,y) coordinate its value from the hologram recorded with the phase pinhole location that corresponds with the desired reconstructed coordinate.

The necessity for a scanning procedure is a main limitation of the above approach, as the scanning is both time demanding and computationally intense. In order to mitigate this burden, a parallelized scanning scheme is hereby proposed. The basic idea is to encode multiple points from a specific plane of interest into a single hologram, rather than just one, by displaying an array of phase pinholes over SLM_2, instead of just a single phase pinhole, as depicted in Fig. 3. Here, square shaped phase pinholes are used, but other shapes (e.g., a circle) may be used as well. The width of a pinhole is represented by w_p, and the distance between pairs of adjacent pinholes (in both x and y directions) is d_p. The width of the scanned area is denoted by w_s, where it is assumed that the scanned area has the form of a square. In a single pinhole scan, the pinhole is laterally shifted throughout the complete scanned area [Fig. 3(a)], requiring at least $\lceil w_s/w_p \rceil$ different scanning points within each scanned line, and usually double of that in order to ensure sufficient overlap; meaning that scanning of a single plane requires around $4\lceil w_s/w_p \rceil^2$ different complex-valued FINCH holograms, each formed

using at least three exposures. In the proposed scanning scheme, however, the amount of required scanning point within each line is reduced to $\lceil (d_p + w_p)/w_p \rceil$. Taking into account sufficient overlap between scanned locations, the total number of complex FINCH holograms per plane is around $4\lceil (d_p + w_p)/w_p \rceil^2$. The reduction factor is:

$$R_f = \frac{4\lceil w_s/w_p \rceil^2}{4\lceil (d_p + w_p)/w_p \rceil^2} \approx \left(\frac{w_s}{d_p + w_p}\right)^2, \tag{9}$$

and may be substantial. For example, a typical scan of the area of an entire SLM of 1,000 × 1,000 pixels in size, using a pinhole of 10 pixels in width, may require around 40,000 complex FINCH holograms. A parallel scan using multiple pinholes, with a distance d_p of 90 pixels would only require around 400 complex FINCH holograms, a reduction of two orders of magnitude. However, the sectioning performance is dependent upon the distance d_p, as demonstrated by the experimental results that follow.
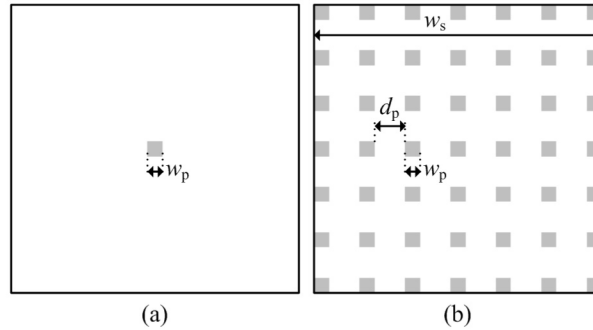

Fig. 3. Masks of (a) a single pinhole and (b) a multiple phase pinholes array.

The above description of FINCH assumes that the SLMs modulate the polarization components of light that are oriented along their active axis in full. In practice, however, this is not the case. Considering Fig. 2, for example, this implies that the beams that are converging towards the image points to the right of the image sensor, a_2, b_2 and c_2, are mostly linear in polarization along the non-active axis of SLM_2, but not entirely. This has little affect on the end result in a non-sectioning FINCH, and even in a sectioning FINCH, where only a single pinhole is used [22]. However, using a multiple phase pinholes array, as here proposed, pronounces the contribution of these unwanted components, mainly because we get contributions between waves that interfere with themselves. To overcome this unwanted contribution, we suggest a procedure that is hereafter referred to as *three-wave interference phase-shifting* (TWIPS). The name is derived from the fact that the interference process may now be considered to be between three waves that originate from a single point source, whereas the phase-shifting process enables to extract a desired cross term between two waves.

2.2 Three-wave interference phase-shifting

Consider the interference of two waves, X_1 and X_2, over the digital sensor plane, where one of the waves is phase-shifted:

$$I_k = \left| e^{i\theta_k} X_1 + X_2 \right|^2 = \left| X_1 \right|^2 + \left| X_2 \right|^2 + e^{i\theta_k} X_1 X_2^* + e^{-i\theta_k} X_1^* X_2. \tag{10}$$

By recording three patterns with different values of $\theta_k = \theta_1, \theta_2, \theta_3$, and calculating [1]:

$$I = I_1 \left(e^{-i\theta_3} - e^{-i\theta_2} \right) + I_2 \left(e^{-i\theta_1} - e^{-i\theta_3} \right) + I_3 \left(e^{-i\theta_2} - e^{-i\theta_1} \right), \tag{11}$$

it is easy to show that Eq. (11) results with

$$I = cX_1 X_2^*, \tag{12}$$

where $c = 2i[\sin(\theta_1 - \theta_3) + \sin(\theta_2 - \theta_1) + \sin(\theta_3 - \theta_2)]$, indicating that the twin-image and zero-order terms in Eq. (10) are eliminated by the above procedure.

Consider now a more general case, in which three waves, W_1, W_2 and W_3 are interfering over the digital sensor plane, meaning that

$$I = |W_1 + W_2 + W_3|^2. \tag{13}$$

We now show that the ability of applying a controllable phase-shift to any two of the three waves can be used to extract any desired cross term between two of the three interfering waves in Eq. (13) (e.g., $W_1 W_2^*$, $W_1 W_3^*$ or $W_2 W_3^*$). Without loss of generality, consider the case of controllable phase-shifts applied to W_1 and W_2 so that

$$I_{k,l} = \left| e^{i\theta_k} W_1 + e^{i\phi_l} W_2 + W_3 \right|^2. \tag{14}$$

Let $X_1 = W_1$ and $X_2 = \exp(i\phi_l)W_2 + W_3$. Based on the procedure described in Eqs. (10)–(12) it is easy to extract the term

$$I_l = X_1 X_2^* = W_1 \left(e^{i\phi_l} W_2 + W_3 \right)^*. \tag{15}$$

If the above procedure is performed with two different values of $\phi_l = \phi_1$, ϕ_2 then

$$W_1 W_2^* = \frac{I_1 - I_2}{e^{-i\phi_1} - e^{-i\phi_2}}, \quad W_1 W_3^* = \frac{e^{i\phi_1} I_1 - e^{i\phi_2} I_2}{e^{i\phi_1} - e^{i\phi_2}}. \tag{16}$$

Extraction of the cross term $W_2 W_3^*$ can be achieved in a similar fashion by first taking $X_1 = W_2$ and $X_2 = \exp(i\theta_k)W_1 + W_3$. The term $X_1 X_2^*$ is then found for two different values of θ_k, each time via phase-shifting over three different values of ϕ_l. In the Appendix, the TWIPS process is described for the case in which a joint phase-shift can be applied simultaneously to two out of three interfering waves, where there is an ability of applying an additional phase-shift to one of these two waves. Then, the TWIPS concept is extended to the more general case of interference between more than three waves. In the following section, the TWIPS concept is described in the context of the example in Fig. 2.

2.3 Three-wave interference in optical sectioning FINCH

In Section 2.1, the phase-shifting procedure in OS-FINCH has been described with the help of Fig. 2, under the assumption that the waves that converge towards the image points to the right of the image sensor are not modulated by SLM_2, upon which the phase pinhole mask is displayed. Even though this is mostly satisfied, in practice, SLM_1 does not modulate the waves that have their polarization components along its active axis in full. This may result, in part, from the limited fill factor of currently available devices. Thus, the waves that converge towards the image point to the right of the image sensor also possess components along the active axis of SLM_2. Even though these components may be relatively small, a way to mitigate their influence should be considered, especially when multiple phase pinholes are used.

Consider the point source c_o in Fig. 4. The interference pattern due to this point source over the image sensor includes several waves. The wave that diverges from the image point c_1, is modulated by both SLMs and can be described as $\exp(i\varphi_k)\{\exp(i\phi_l)S(C_1)C_1 + [1 - S(C_1)]C_1\}$, where φ_k and ϕ_l are phase-shifting parameters controlled via SLM_1 and SLM_2, respectively. The latter is only set within the phase pinhole regions on SLM_2 [Fig. 3], while the former is set on SLM_1 entirely. The support function $S(C_1)$ is defined in Section 2.1

following Eq. (3). The wave that converges towards the image point c_2, has dominant polarization components along the non-active axis of SLM_2, which can be denoted as C_2, and undesired components along the active axis of SLM_2, described as $\exp(i\phi_l)S(C_3)C_3 + [1 - S(C_3)]C_3$, where part of the wave is phase-shifted when passed through the phase pinhole, as indicated by the support function $S(C_3)$. Other components that may exist are assumed to be negligible and are neglected from the analysis. Thus, the recorded interference pattern for the point source c_o can be written as:

$$I_{k,l}\left(x,y;\{c_o\}\right)=\left|e^{i\varphi_k}\left\{e^{i\phi_l}S(C_1)C_1+\left[1-S(C_1)\right]C_1\right\}+C_2+e^{i\phi_l}S(C_3)C_3+\left[1-S(C_3)\right]C_3\right|^2 \quad (17)$$
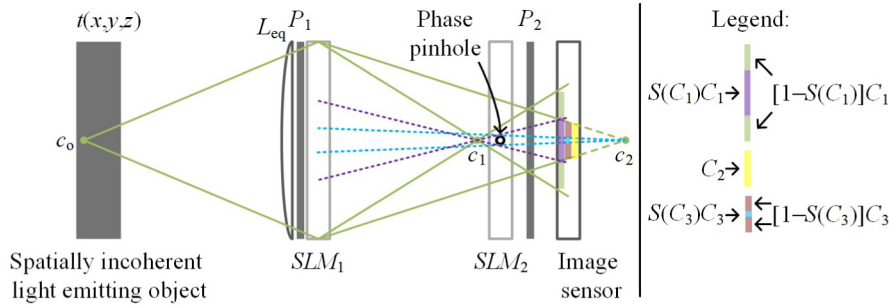

Fig. 4. Wave interference in optical sectioning FINCH: L_{eq}, an equivalent lens, representing both the objective lens L_o and the converging lens L_c (Fig. 1); P_1 and P_2, polarizers; SLM_1 and SLM_2, spatial light modulators; c_o, a point source; c_1 and c_2, point source images; C_1, the wave that diverges from the image point c_1 over the image sensor plane, composed of parts that pass through the phase pinhole $[S(C_1)C_1]$ and parts that do not $\{[1 - S(C_1)C_1]\}$; C_2, the wave that converges towards the image point c_2 over the image sensor plane and is not modulated by SLM_2; C_3, the wave that converges towards the image point c_2 over the image sensor plane and is modulated by SLM_2, composed of parts that pass through the phase pinhole $[S(C_3)C_3]$ and parts that do not $\{[1 - S(C_3)C_3]\}$. For simplicity, only a single phase pinhole is shown.

The form of Eq. (17) may be considered as the interference of five waves. Taking into account that the axicon displayed over SLM_2 deflects two of them from reaching the image sensor, Eq. (17) can be reduced to:

$$I_{k,l}\left(x,y;\{c_o\}\right)=\left|e^{i(\phi_l+\varphi_k)}S(C_1)C_1+e^{i\phi_l}S(C_3)C_3+C_2\right|^2. \quad (18)$$

Note that the form of the above equation is similar in form to Eq. (19) in the Appendix. Therefore, the TWIPS procedure described in Eq. (20), Eq. (21) and the left-hand-side of Eq. (22) can be used to extract the cross term $S(C_1)C_1C_2^*$ using a total of six exposures. This is the exact same term that represents the point source c_o in Eq. (4), indicating that the suggested method can effectively deal with the undesired waves that are included in the analysis.

3. Experiments

An experimental setup based on the schematic of Fig. 5 was implemented. It is based directly upon the configuration of Fig. 1, but uses reflective SLMs (Holoeye PLUTO, 1920 × 1080 pixels, 8 μm pixel pitch, phase-only modulation) instead of transmissive ones. A beam splitter was inserted next to each of the SLMs, so that they can be used like transmissive type SLMs. For simplicity, the two lenses L_o and L_c were replaced by a single equivalent lens L_{eq} of focal length $f_{eq} = 20$ cm, representing an objective lens L_o of focal length $f_o = 23.08$ cm and a converging lens L_c of focal length $f_c = 150$ cm. The distance between the lens L_{eq} and SLM_1 was set to 10 cm. SLM_2 and the image sensor (Hamamatsu ORCA-Flash4.0 V2 Digital CMOS, 2048 × 2048 pixels, 6.5μm pixel pitch, monochrome) were positioned at distances of 66.32 cm and 90 cm away from SLM_1, respectively. Two resolution charts were combined using a beam combiner into a 1 cm thick object. A negative 1951 United States Air Force

(USAF) resolution chart was placed at a distance f_o in front of the lens L_{eq}, while a negative National Bureau of Standards (NBS) 1963A was placed at a distance of $f_o + 1$ cm = 24.08 cm in front of the same lens. Each resolution chart was back-illuminated using an LED (Thorlabs LED635L, 170 mW, central wave length of λ = 635 nm, full width at half maximum $\Delta\lambda$ = 15 nm). The exposure time of the image sensor was set to 80 ms per grabbed frame.

At first, regular (non-sectioning) FINCH holograms were recorded. The mask of the second SLM, SLM_2, was set to a uniform phase-modulation value of zero, electronically transforming the setup into a regular FINCH configuration. Two FINCH holograms were recorded, each calculated according to Eq. (11) from three exposures with difference phase-shifting values of $\theta_1 = 0°$, $\theta_2 = 120°$ and $\theta_3 = 240°$. The first and second holograms were recorded with the USAF and NBS targets imaged upon SLM_2, respectively. Reconstruction results from the first hologram, showing the USAF and NBS charts in planes of best focus are shown in Figs. 6(a) and 6(b), respectively. Note that details of the two charts are not easily resolved in regions within the two charts overlap. In the case of the second hologram, the USAF and NBS charts appear in best focus simultaneously, as shown in the reconstruction in Fig. 6(c). These results are brought here to allow comparison with the results from an optical sectioning capable FINCH setup that follow.
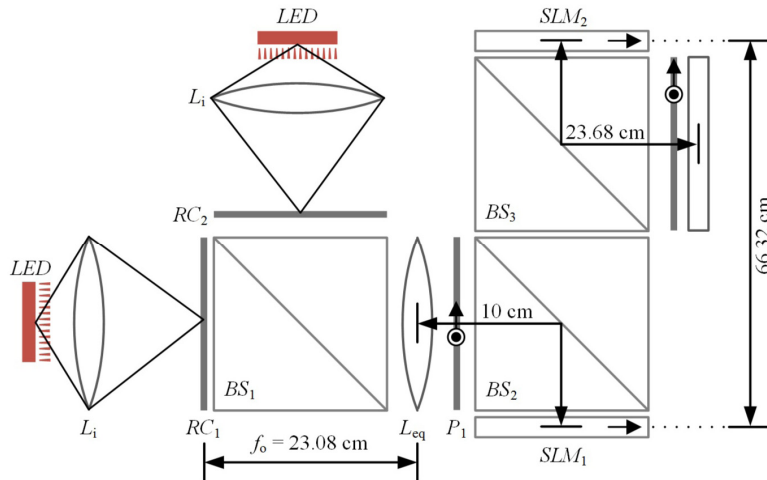

Fig. 5. Optical sectioning FINCH experimental setup: L_{eq}, an equivalent lens, representing both the objective lens L_o and the converging lens L_c (Fig. 1); P_1 and P_2, polarizers; SLM_1 and SLM_2, spatial light modulators; RC_1 and RC_2, resolution charts; BS_1, BS_2 and BS_3, beam splitters (BS_1 is used as a beam combiner); LEDs, light emitting diodes; L_is, illumination lenses.
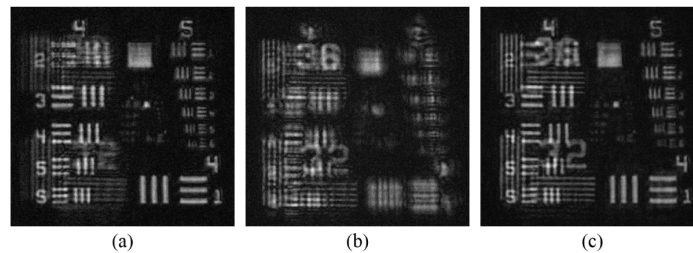

(a)   (b)   (c)

Fig. 6. Reconstructions of non-sectioning FINCH holograms at plane of best focus for 1951 USAF chart [(a) and (c)] and NBS 1963A chart [(b) and (c)]. (a) and (b) were reconstructed from the first hologram, recorded with the 1951 USAF chart imaged to the plane of SLM_2. (c) was reconstructed from the second hologram, recorded with the NBS 1963A chart imaged to the plane of SLM_2.

In the optical sectioning experiments, each of the two planes of interest (the two resolution charts) were first scanned using a square shaped phase pinhole of 88 μm in width (i.e., 11 pixels over 11 pixels in size). The scan was performed on a grid of size 101 × 101 points, with the phase pinhole shifted in jumps of 40 μm, enabling sufficient overlap between imaged positions. For each pinhole position, a complex FINCH hologram was calculated from six different exposures, based on the procedure described in Section 2.3, where SLM_1 was set with $\varphi_1 = 0°$, letting the phase pinhole, which is displayed on SLM_2, take the values $\phi_1 = 0°$, $\phi_2 = 120°$ and $\phi_3 = 240°$, or with $\varphi_2 = 180°$, again letting the phase pinhole take the three values of $\phi_1 = 0°$, $\phi_2 = 120°$ and $\phi_3 = 240°$. Then, scanning using multiple phase pinholes, in parallel, was tested. The spacing between adjacent phase pinholes (in both x and y direction) was set to values of $88 \times g$ μm, with $g = 1 .. 15$, implying spacing of 1 to 15 pinholes in width, between pinholes. It should be emphasized that: (1) a trial to perform a regular phase-shifting of three exposures, according to [22], does not yield acceptable results when multiple phase pinholes are displayed; (2) a mask of an axicon that occupy the phase pinhole(s) surrounding(s) was indeed used in the presented experiments and yielded better results than the case of working without the axicon; (3) the exposure time of 80 ms per grabbed frame indicates that a single complex FINCH hologram requires roughly 0.5 s for its recording. In practice, the total time required for the recording was about 2 s, a figure which can be reduced with tighter synchronization.
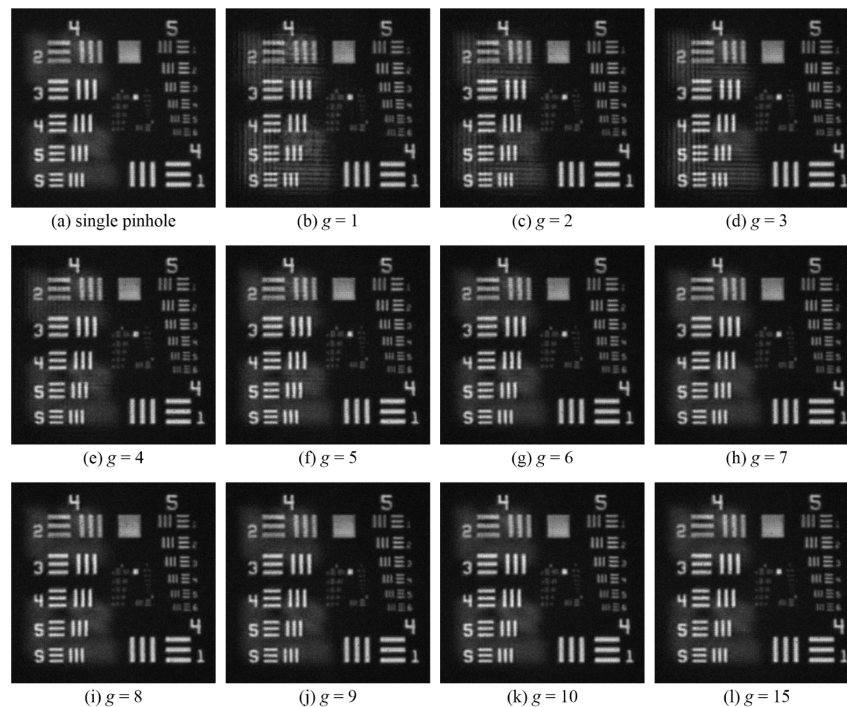

Fig. 7. Reconstructions of optical sectioning FINCH holograms at plane of best focus for the 1951 USAF chart. In (a) a single phase pinhole was used, while in (b)–(l) multiple phase pinholes were used in parallel, where the spacing between adjacent pinholes (in x and y directions) was set to $88 \times g$ μm, starting with $g = 1$ in (b) and ending with $g = 15$ in (l). Results for $g = 11 .. 14$ are not presented, due to lack of visible difference.

Reconstruction results, based on the procedure described in Section 2, for the holograms recorded with the 1951 USAF resolution chart as the plane of interest, are presented in Fig. 7. Visual comparison of the reconstruction from the hologram set acquired using only a single phase pinhole [Fig. 7(a)] with the results of multiple phase pinholes, starting with the spacing of a single pinhole in Fig. 7(b) through spacing of 15 pinholes in Fig. 7(l), reveals gradual

improvement in the sectioning performance that increases with the spacing between the pinholes, until a spacing of 7 pinholes is reached [Fig. 7(h)]. From that point, any increase in the spacing between pinholes does not reveal visual improvement in the sectioning results [Figs. 7(h)–7(l)], which resemble the performance in the case of a single pinhole [Fig. 7(a)]. That is, there is a trade-off between the complexity of the scan and the sectioning performance. We note that by visual comparison there is a clear improvement even between the highly parallelized (with $g = 1$) optical sectioning FINCH in Fig. 7(b) and the non-sectioning FINCH in Fig. 6(a). To quantify the results, the mean squared error (MSE) was calculated between the amplitude of the reconstruction in Fig. 7(a) and the amplitude of the reconstructions in Figs. 7(b)–7(l). The cases of $g = 11 .. 14$, which are not presented in Fig. 7, for brevity, were also included in the MSE calculations. Further, the non-sectioning FINCH reconstruction in Fig. 6(a) is considered to represent the case of $g = 0$. The results are presented in Fig. 8, and are fairly consistent with the visual inspection. Taking into consideration that Fig. 7(a) was generated using 10,102 complex FINCH holograms, Fig. 7(i) using more than an order of a magnitude less (400 complex holograms), and Fig. 7(b) using only 25 complex holograms, it is clear that in practice it may be necessary to balance between the required sectioning and the time that is available for the process (here, the total time taken for scanning a single plane varied between few seconds to several hours, depending on the value of g). Still, the scanning time may be substantially decreased, without impairing the sectioning performance. Reconstruction results for the NBS 1963A resolution chart are presented in Fig. 9, with the MSE graph presented in Fig. 10. The previous conclusions are further supported by the results.
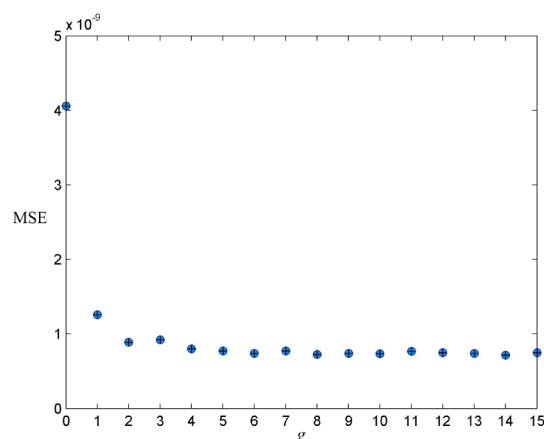

Fig. 8. Amplitude mean squared error (MSE) between the reconstruction in Fig. 7(a), where scanning was performed using a single pinhole, and the reconstructions in Figs. 7(b) through 7(l), where parallel mode scanning was performed using multiple phase pinholes, with g values of 1 through 15, respectively, indicating the gap between adjacent phase pinhole, in integer multiplies of the width of a single pinhole. The result for g value of 0 is against the reconstruction of Fig. 6(a), from a non-sectioning FINCH hologram.

Finally, to demonstrate the necessity of the TWIPS procedure, Fig. 11 presents the reconstructions of two different complex FINCH hologram, acquired with g values of 15 and 1, starting with a relatively low number of in-parallel phase pinholes, and ending with a relatively large number. The reconstructions of the complex FINCH holograms, using a regular phase-shifting procedure with three different exposures, are presented in Figs. 11(a) and 11(b). Besides showing small fractions of the 1951 USAF resolution chart that fall within the phase pinholes, noise-like artifacts are also visible in the reconstructions. The higher the number of in-parallel phase pinholes (indicated by lower values of g), the more prominent are the artifacts. Using TWIPS, however, where each complex FINCH hologram requires a total of six different exposures, these artifacts are eliminated, as shown in Figs. 11(c) and 11(d).

Thus, the contribution of TWIPS is apparent, and its necessity for the successful utilization of the suggested parallel scanning scheme in OS-FINCH is demonstrated, especially when the degree of parallelism is high.
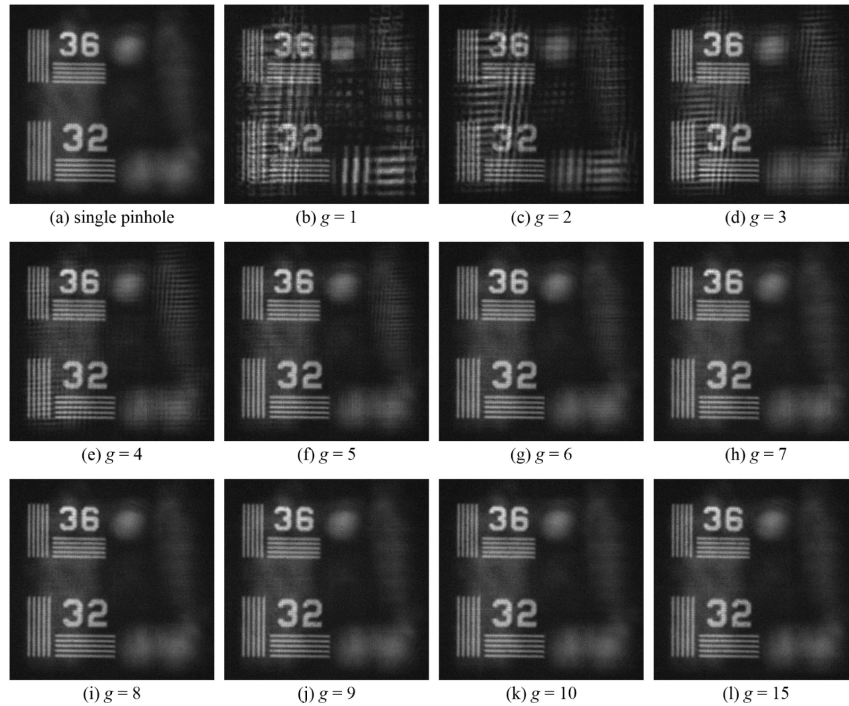

Fig. 9. Reconstructions of optical sectioning FINCH holograms at plane of best focus for the NBS 1963A chart. In (a) a single phase pinhole was used, while in (b)–(l) multiple phase pinholes were used in parallel, where the spacing between adjacent pinholes (in x and y directions) was set to $88 \times g$ μm, starting with $g = 1$ in (b) and ending with $g = 15$ in (l). Results for $g = 11 .. 14$ are not presented, due to lack of visible difference.
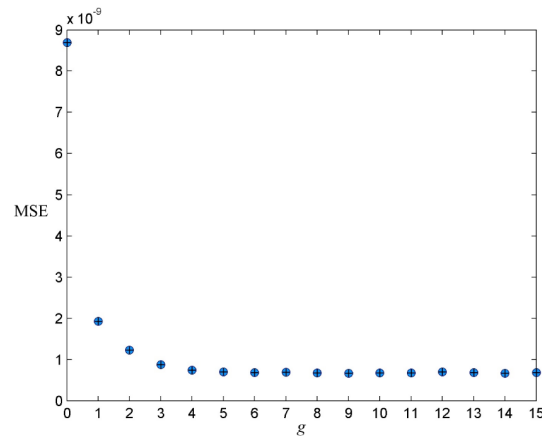

Fig. 10. Amplitude mean squared error (MSE) between the reconstruction in Fig. 9(a), where scanning was performed using a single pinhole, and the reconstructions in Figs. 9(b) through 9(l), where parallel mode scanning was performed using multiple phase pinholes, with g values of 1 through 15, respectively, indicating the gap between adjacent phase pinhole, in integer multiplies of the width of a single pinhole. The result for g value of 0 is against the reconstruction of Fig. 6(c), from a non-sectioning FINCH hologram.

(a) $g = 15$, regular phase-shifting (b) $g = 1$, regular phase-shifting (c) $g = 15$, TWIPS (d) $g = 1$, TWIPS
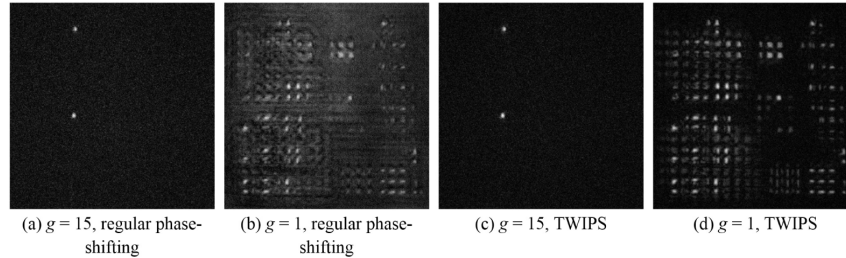
Fig. 11. Regular phase-shifting vs. TWIPS in OS-FINCH. In (a) and (b) hologram reconstructions from complex FINCH holograms are shown, each calculated using a regular phase-shifting procedure, based on three different exposures. Each of the holograms was recorded for a single position of multiple phase pinholes, with the distance between adjacent phase pinholes set to $88 \times g$ μm, with $g = 15$ (a) and $g = 1$ (b). (c) and (d) are the TWIPS equivalents of (a) and (b), respectively, where each complex FINCH hologram was calculated based on six different exposures. Using regular phase-shifting, it is evident that the larger the number of phase pinholes, comparing (a) and (b), the more prominent are the noise-like artifacts in the reconstructions. In contrast, these artifacts are not noticed in the TWIPS reconstructions of (c) and (d).

4. Summary and conclusions

A new scanning procedure in an optical sectioning FINCH configuration has been presented. The procedure offers parallel-mode scanning capable of imaging a large number of points in an examined object plane simultaneously. This is achieved through the use of multiple phase pinholes. The speed gain is dependent upon the specific characteristics of the object. In the presented experimental results, a speedup of roughly one order of magnitude has been achieved, without any deterioration of the sectioning capabilities. Higher speedups are possible, but require a balance between the desired speed and the quality of the sectioning.

The use of multiple phase pinholes based scan is more sensitive to some of the nonidealities of currently available SLM devices, in comparison to the situation of using just a single phase pinhole. The suggested analysis of the case suggests that for a single point source, more than two waves are involved in the interference process. This is dealt with through a phase-shifting procedure which is referred to as TWIPS. The procedure effectively eliminates any of the unwanted interference terms, offering successful implementation of the suggested parallel-mode scan. TWIPS is discussed not only in the context of FINCH, but also in a broader and more general sense, so that it may readily be adapted to other systems as well, if necessary.

Overall, in OS-FINCH the sectioning is done only in the image plane, where the phase pinholes operate. Therefore, on the one hand, the sectioning performance of OS-FINCH are expected to be inferior to that of a conventional confocal microscope. This conclusion is valid at least until a confocal version of the proposed OS-FINCH system is demonstrated, in which a matching pinhole array will be used to illuminate the speciemen. On the other hand, it should be noted that the present OS-FINCH is suitable to imaging situations in which there is no access or possibility to illuminate speciemens with a beam array, like in confocal microscopy. Another advantage of OS-FINCH over the common confocal microscopes equipped with a spinning disk [24], is that in the OS-FINCH there are not any moving parts. The entire 3-D scanning is electronic rather than mechanical, and therefore the scanning may be potentially faster and more robust.

Appendix

The case in which three waves, W_1, W_2 and W_3, are interfering over the digital sensor plane is considered in this appendix. This time, it is assumed that a simultaneous phase-shift can be applied to two of these waves, say W_1 and W_2, and that an additional phase-shift can be separately applied to W_1. This is in contrast to the previously discussed case, in which two different phase-shifts could be applied separately to W_1 and W_2. Thus, the intensity of the interference between the waves is:

$$I_{k,l} = \left| e^{i(\phi_l + \varphi_k)} W_1 + e^{i\phi_l} W_2 + W_3 \right|^2,$$ (19)

where the phase-shifting parameter ϕ_l accounts for both W_1 and W_2 and the parameter φ_k to W_1 alone. Define $\varphi_k = \theta_k - \phi_l$, Eq. (19) becomes similar to Eq. (14), and thus any desired cross term between the three interfering waves can be extracted, following Eqs. (14)–(16). This definition of φ_k can be considered as a way to compensate for any value of ϕ_l, effectively allowing separate phase-shifting control over W_1 and W_2. An alternative procedure that does not use this technique of compensation is now presented.

Let $\theta_l = \phi_l$, $X_1 = \exp(i\varphi_k)W_1 + W_2$ and $X_2 = W_3$. Equation (19) can be rewritten as:

$$I_{k,l} = \left| e^{i\theta_l} X_1 + X_2 \right|^2 = \left| X_1 \right|^2 + \left| X_2 \right|^2 + e^{i\theta_l} X_1 X_2^* + e^{-i\theta_l} X_1^* X_2.$$ (20)

Following a procedure similar to the one described in Eqs. (10)–(12), phase-shifting over three different values of θ_l, it is easy to extract from Eq. (20) the cross term

$$I_k = X_1 X_2^* = \left(e^{i\varphi_k} W_1 + W_2 \right) W_3^*.$$ (21)

Performing the above for two different values of $\varphi_k = \varphi_1, \varphi_2$, the following cross terms of Eq. (19) can be extracted:

$$W_1 W_3^* = (I_1 - I_2) \big/ \left(e^{i\varphi_1} - e^{i\varphi_2} \right), \quad W_2 W_3^* = \left(e^{-i\varphi_1} I_1 - e^{-i\varphi_2} I_2 \right) \big/ \left(e^{-i\varphi_1} - e^{-i\varphi_2} \right).$$ (22)

Alternatively, let $\theta_k = \varphi_k$, $X_1 = \exp(i\phi_l)W_1$ and $X_2 = \exp(i\phi_l)W_2 + W_3$. Equation (19) can be rewritten as:

$$I_{k,l} = \left| e^{i\theta_k} X_1 + X_2 \right|^2 = \left| X_1 \right|^2 + \left| X_2 \right|^2 + e^{i\theta_k} X_1 X_2^* + e^{-i\theta_k} X_1^* X_2.$$ (23)

Phase-shifting over three different values of θ_k, it is easy to extract from Eq. (23) the cross term

$$I_l = X_1 X_2^* = e^{i\phi_l} W_1 \left(e^{i\phi_l} W_2 + W_3 \right)^* = W_1 \left(W_2 + e^{-i\phi_l} W_3 \right)^*.$$ (24)

Implementing the above for two different values of $\phi_l = \phi_1, \phi_2$, the following cross terms of Eq. (19) can be extracted:

$$W_1 W_2^* = \left(e^{-i\phi_1} I_1 - e^{-i\phi_2} I_2 \right) \big/ \left(e^{-i\phi_1} - e^{-i\phi_2} \right), \quad W_1 W_3^* = (I_1 - I_2) \big/ \left(e^{i\phi_1} - e^{i\phi_2} \right).$$ (25)

Finally, consider a more general case, in which multiple waves, $W_1, W_2 .. W_p$, are interfering over the digital sensor plane, so that

$$I = \left| W_1 + W_2 + .. + W_p \right|^2.$$ (26)

We now show that the ability of applying a controllable phase-shift to two of the waves, say W_m and W_n from $W_1, W_2 .. W_p$, can be used to extract a desired cross term, $W_m W_n^*$, from Eq. (26), so that

$$I_{k,l} = \left| W_1 + .. + W_{m-1} + e^{i\theta_k} W_m + W_{m+1} + .. + W_{n-1} + e^{i\phi_l} W_n + W_{n+1} + .. + W_p \right|^2.$$ (27)

Let $X_1 = W_m$ and $X_2 = W_1 + .. + W_{m-1} + W_{m+1} + .. + \exp(i\phi_l)W_n + .. + W_p$. Equation (27) can be rewritten in the form of Eq. (23). Phase-shifting over three different values of θ_k, based on the procedure described in Eqs. (10)–(12) it is easy to extract the term

$$I_l = X_1 X_2^* = W_m \left(W_1 + .. + W_{m-1} + W_{m+1} + .. + e^{i\phi_l} W_n + .. + W_p \right)^*.$$ (28)

If the above procedure is performed with two different values of $\phi_l = \phi_1, \phi_2$ then

$$I = (I_1 - I_2) \big/ \left(e^{-i\phi_1} - e^{-i\phi_2} \right) = W_m W_n^*.$$ (29)

Acknowledgment